ELSEVIER

Journal of Hydrology 267 (2002) 125–146

Journal of Hydrology

www.elsevier.com/locate/jhydrol

Imaging and characterisation of subsurface solute transport using electrical resistivity tomography (ERT) and equivalent transport models

Andreas Kemna[a,*], Jan Vanderborght[a], Bernd Kulessa[b], Harry Vereecken[a]

[a]*Institute of Chemistry and Dynamics of the Geosphere, Forschungszentrum Jülich GmbH, 52425 Jülich, Germany*
[b]*Environmental Engineering Research Centre, School of Civil Engineering, Queen's University of Belfast, Belfast, BT9 5AG, Northern Ireland*

Abstract

We assess the usefulness of electrical resistivity tomography (ERT) in imaging and characterising subsurface solute transport in heterogeneous unconfined aquifers. A field tracer experiment was conducted at the Krauthausen test site, Germany. The spatial and temporal evolution of the injected NaBr solute plume was monitored in a 2D ERT image plane located downstream of the injection well for 90 days. Since ERT maps changes in bulk electrical conductivity, the reconstructed images at selected time intervals are first converted to solute concentration maps by postulating a linear relation. The concentration maps are then analysed using an equivalent convection–dispersion model (CDM), which conceptualises the aquifer as a homogeneous medium with a uniform mean flow velocity. As demonstrated by associated synthetic model studies, ERT resolution in terms of recovered equivalent dispersivities is limited due to spatial smoothing inherent to the imaging algorithm. Since for heterogeneous media, local concentrations within the plume deviate from those predicted by the equivalent CDM, we also interpret the ERT-derived pixel breakthrough curves in terms of an equivalent stream-tube model (STM). The STM represents transport in the aquifer by a set of 1D convection–dispersion processes, allowing the degree of mixing and the heterogeneity of transport within the plume to be quantified. We believe that the observed tracer plume is satisfactorily described by the equivalent CDM, probably because the tracer plume was small relative to the heterogeneity scale of the aquifer. Even though application of the STM revealed some deviation from the ideal homogeneous case, the equivalent dispersivity in the STM matches the longitudinal dispersivity of the CDM closely, consistent with predominantly homogeneous mixing. However, the STM analysis illustrates how ERT results can be used to quantify the variability of parameters relevant to flow and transport in heterogeneous aquifers.

Keywords: Aquifers; Electrical conductivity; Electrical methods; Solute transport

1. Introduction

Monitoring solute plumes during tracer tests in heterogeneous aquifers is often problematic since the trajectory of the tracer plume and its exact spatial extent at any point of time are unknown. As a consequence, it is difficult to capture the position and exact shape of a tracer plume using a grid of multilevel observation wells. In contrast, electrical resistivity tomography (ERT) allows imaging of solute concentrations, and thus tracer migration, in 2D or 3D at markedly higher spatial resolution. The use of electrical methods for monitoring hydrological

* Corresponding author. Tel.: +49-2461-61-4077; fax: +49-2461-61-2518.
E-mail addresses: a.kemna@fz-juelich.de (A. Kemna), j.vanderborght@fz-juelich.de (J. Vanderborght), b.kulessa@gub.ac.uk (B. Kulessa), h.vereecken@fz-juelich.de (H. Vereecken).

0022-1694/02/$ - see front matter
PII: S0022-1694(02)00145-2

processes in the subsurface is well documented in the literature. Earlier studies include monitoring of groundwater flow by profiling or mapping the electrical response to an injected saline tracer, either solely from the ground surface (White, 1988, 1994; Osiensky and Donaldson, 1995; Morris et al., 1996) or in boreholes (Bevc and Morrison, 1991). In recent years sophisticated ERT inversion techniques have been developed, making tomographic imaging of subsurface fluid movement possible. Successful qualitative applications have been reported for porous (Daily et al., 1992, 1995) and fractured (Slater et al., 1997) media. In contrast, quantitative assessment of transport characteristics in soils and rocks from ERT data is poorly documented (Binley et al., 1996; Slater et al., 2000).

We report the results of a field tracer experiment and associated synthetic modelling to elucidate the value of ERT for imaging and characterising subsurface solute transport in a heterogeneous sand and gravel aquifer. We focus on the derivation of solute concentration maps from the ERT measurements and their analysis using dedicated transport models.

The first objective of our study is to bring forward a set of a priori assumptions needed for conversion of ERT measurements to solute concentrations. First, regularisation is necessary to constrain the number of possible solutions to the nonunique ERT inverse problem. Choice of the regularisation method is not defined by the data, but is instead based on a priori information, best guesses, and/or experience. Second, for cross-borehole electrode arrangements data sampling, and thus spatial resolution, is commonly markedly enhanced in the vertical compared to the horizontal direction. Third, the calibration relation relating bulk subsurface electrical conductivity, as reflected by the ERT data, to tracer concentration depends on various textural and physico-chemical properties of the soil/rock–groundwater system. This relation is often variable in space and cannot be determined for each location in the ERT image plane without additional assumptions.

The second objective is to illustrate how concentration maps obtained from ERT can be used to quantify spreading of the solute plume resulting from flow heterogeneities in the longitudinal (i.e. parallel to the flow axis) and transverse (i.e. perpendicular to the flow axis) directions. Spreading is quantified in terms of dispersivity parameters in an equivalent convection–dispersion model (CDM). Such CDMs consider the actual transport properties in the heterogeneous medium in terms of equivalent transport properties in an idealised homogeneous porous medium. In this idealised medium, flow and advection velocities are uniform and dispersion of the solute plume is described as a Fickian or gradient-driven process using a constant dispersion tensor. The equivalent transport parameters are defined such that the predicted concentrations in the equivalent medium match the concentration distribution in the actual, heterogeneous medium. Following injection, the tracer distribution is distorted by flow heterogeneities and anomalous solute concentrations within the plume, causing noticeable deviations from the concentrations predicted by the equivalent CDM. The CDM represents a transport process with a maximum homogenisation or mixing of solute mass within the plume (Kitanidis, 1994). The degree of mixing controls the reaction rates between different substances and is therefore a key process for degradation and remediation. Overestimating mixing or homogenisation leads to an overestimation of effective reaction rates which are calculated from local concentrations predicted by an equivalent CDM (Ginn et al., 1995). In order to quantify the actual degree of mixing and the degree of transport heterogeneity within the solute plume, we use a stream-tube model (STM). The STM represents transport in the aquifer by a set of 1D transport processes (Bresler and Dagan, 1981; Simmons, 1982). The heterogeneity of transport is represented by the variability of advection velocities within the population of stream tubes. Mixing is represented by an equivalent local longitudinal dispersion process within the stream tubes. The equivalent local dispersivity, which quantifies the mixing process within these tubes, is derived from locally measured time series of concentrations (Cirpka and Kitanidis, 2000a,b; Vanderborght and Vereecken, 2001).

2. Setup

2.1. Field experiment

The tracer experiment was carried out in a

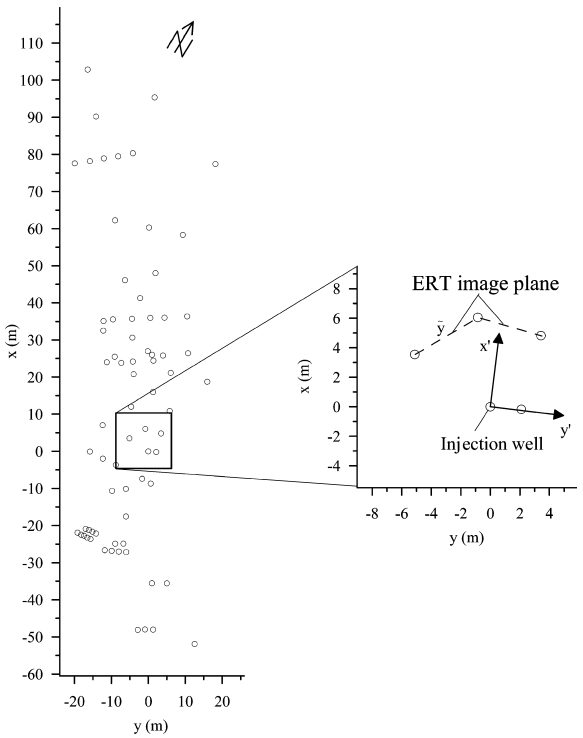

Fig. 1. Map of Krauthausen test site (central area) showing distribution of monitoring wells (left) and location of boreholes selected for ERT imaging and tracer injection (right). The original coordinate system is denoted by (x, y), whereas (x', y') is the coordinate system that coincides with the mean flow direction between the injection well and the ERT image plane. The coordinate $\tilde{y}$ corresponds with the horizontal distance along the two adjacent inter-borehole planes defining the ERT image plane.

heterogeneous aquifer at the Krauthausen test site of the Forschungszentrum Jülich GmbH (Germany). A detailed description of the site is given in Vereecken et al. (2000). The base of the unconfined aquifer consists of thin layers of clay and silt that extend from 11 to 13 m below surface (b.s.). The aquifer may broadly be divided into two layers: a bottom layer consisting of sand and gravel mixtures extending from 4.5 to 11 m b.s., and an overlying layer characterised by brown gravel extending from 1.3 to 4.5 m b.s. The groundwater table typically fluctuates between 2.5 m b.s. in summer and 1 m b.s. in winter. On top of the brown gravel layer, a loess layer has been deposited in which a soil profile with gleyic properties has developed.

For monitoring purposes, 72 observation wells (5 cm diameter) were installed at the site (Fig. 1). Of these 72 wells, 58 are equipped with 24 PE tubes each (0.5 cm diameter), allowing multilevel groundwater sampling every 0.3 m down to a depth of 10 m (Vereecken et al., 2000). Based on the knowledge about horizontal hydraulic flow field from previous studies (Vereecken et al., 2000), four boreholes were selected for the tracer experiment: one for tracer injection and, downstream thereof, three for ERT imaging (Fig. 1). The upstream borehole is filtered over a 1 m long section between 6 and 7 m b.s., while the three downstream boreholes are filtered over a 7 m long section between 3 and 10 m b.s. Each ERT borehole was equipped with 13 stainless steel electrodes installed at 0.5 m intervals between 3.2 and 9.2 m b.s. Additional electrodes were installed at

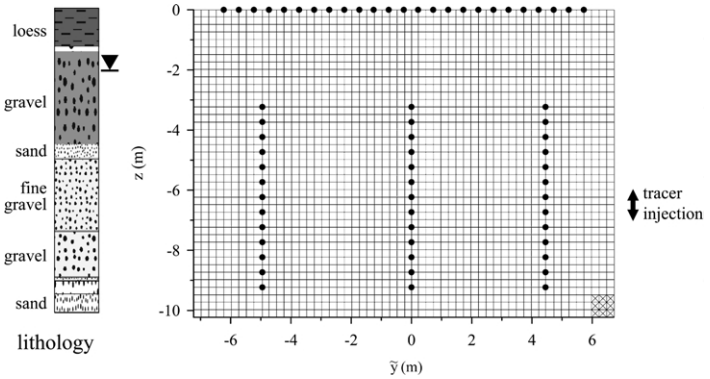

Fig. 2. Cross-sectional view of the experimental setup at the Krauthausen test site, showing electrode arrangement (solid circles) in the two adjacent inter-borehole planes (Fig. 1) and the corresponding parameterisation of the composed ERT image plane as used in the tomographic inversion (the underlying finite-element discretisation is indicated in the bottom right corner of the grid). The lithologic situation at the site and the depth of tracer injection (out of the displayed section) are indicated, respectively, on the left and on the right-hand side.

the soil surface (at 0.5 m intervals) along the ERT image plane defined by the two adjacent inter-borehole planes. This resulted in a total of 64 electrodes used for ERT data acquisition. The electrode arrangement in the composed ERT image plane is shown in Fig. 2, together with its parameterisation into 2296 model cells used in the tomographic inversion. Also indicated in Fig. 2 is the given lithologic situation at the site and the groundwater level during the experiment (2 m b.s.).

On 19 October 2000, 2000 l of NaBr tracer solution were injected into the aquifer at 6–7 m depth (the filtered section of the injection borehole) over a period of 4 h at a rate of 500 l/h. The Br^- concentration of the injected solution was 11.6 g/l. The tracer concentration was chosen as a reasonable compromise between high electrical and low density contrast. Naturally, the former criterion is desirable to ensure detectability of the solute plume by means of ERT. However, sinking of the plume due to gravity effects is usually unwanted in order to allow attributing the evolution of the plume exclusively to natural hydraulic gradients. Moreover, in the present case, significant sinking of the plume had been considered as a severe problem since tracer injection was relatively deep compared with the vertical extension of the ERT image plane (Fig. 2).

ERT data were collected over 90 days following tracer injection. Initial sampling rate was high at one survey (frame) per day, but decreased with electrical response over time. We focus on the first 13 ERT frames, where principal tracer breakthrough occurred. These frames were measured between day 0 (background frame), immediately before tracer injection, and day 18 after injection. For each frame, the same set of dipole–dipole data was collected, comprising about 1900 individual transfer resistance (voltage to current ratio) measurements. We used a circulating, so-called 'skip one' schedule, that is all possible dipole–dipole configurations with a fixed dipole 'length' of two electrode spacings (i.e. one electrode is 'skipped'). More details related to this measurement schedule are given by, for instance, Slater et al. (2000). With a view to the application of a 2D imaging algorithm, only electrode configurations belonging to the same inter-borehole plane of the (composed) ERT image plane were considered.

2.2. Synthetic experiment

In order to assess the resolution of the ERT-derived electrical conductivity and solute concentration maps for the electrode arrangement used in the field tracer test, we carried out a numerical experiment. In this experiment, synthetic concentration distributions were generated in the ERT image plane. Assuming absolute changes in solute concentration to be proportional to relative changes in (bulk) electrical conductivity (this issue is addressed in Section 3.4), these concentration models can be readily identified with electrical conductivity distributions. For these (2D) model distributions, synthetic resistance data were calculated for the same measurement schedule as in the field survey. Gaussian distributed random noise was imposed on the modelled resistance data with a magnitude (standard deviation) of 3%, following our estimate of actual field data noise (with respect to temporal changes). For each data set, an independent ensemble of random numbers was used. Subsequently, the model distributions were reconstructed from the noisy data. Details on the forward modelling and the reconstruction algorithm are given below (Sections 3.1 and 3.2).

Eight different electrical conductivity/concentration models were considered. The distributions were generated starting from a 2.75 m by 1.25 m rectangular anomaly, representing the initial state of a diffusing solute plume. The rectangle was positioned between the middle and right-hand side boreholes in the ERT image plane, with the horizontal centre of the rectangle located 1.845 m from the middle borehole. Two different vertical positions of the rectangle were considered: one with the vertical centre of the rectangle at −6.105 m ('centre position') and one at −9.105 m ('deep position') (Fig. 5(a)–(d)). The initial electrical conductivity was assumed to be 10 mS/m outside and 43 mS/m within the rectangle. The latter value was chosen such that the associated tracer mass within the rectangular area is similar to the tracer mass that was actually observed in the field experiment when the peak concentration crossed the ERT plane. The deep position was chosen in accordance with the position of the tracer plume breakthrough as observed in the field (Fig. 9(a)–(e)). Unfortunately, the plume crossed the ERT plane in a

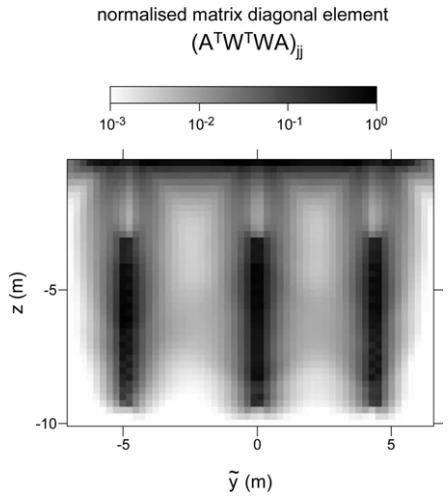

Fig. 3. Typical map of accumulated sensitivity (Eq. (10)) in the ERT image plane for the electrode arrangement and measurement schedule used in this study.

region with a low sensitivity (Fig. 3). In order to evaluate the capability of the ERT method for a tracer breakthrough in the high sensitive region of the image plane, in addition the centre position was considered. The initial solute concentration was allowed to diffuse out of the rectangle into the surrounding area in the image plane over a period of 5 days in order to simulate transverse dispersion of a migrating tracer plume. For each rectangle position, four different diffusion rates were considered corresponding to the dispersion coefficients 0.01, 0.04, 0.1, and 0.25 m^2/d.

The resolution of the ERT method was evaluated on the basis of the dispersion coefficients that were derived from the reconstructed concentration distributions. These dispersion coefficients correspond with the associated diffusion coefficients which were obtained by fitting the analytical solution of the 2D diffusion equation to the reconstructed concentration maps. Although the diffusion process that was considered to generate the input concentration distributions was isotropic, we allowed the fitted model to account for an anisotropic process. Consequently, we fitted a horizontal and a vertical diffusion coefficient, in turn associated with the horizontal and vertical transverse dispersion of a migrating solute plume. To avoid unnecessary confusion, however, we will hereafter consistently refer to the coefficients as dispersion coefficients.

3. Methods

3.1. ERT imaging

Since in this paper, application of ERT is confined to a single vertical image plane, we use a 2D imaging approach for simplicity by assuming that the subsurface bulk electrical conductivity distribution, $\sigma_b(\tilde{x}, \tilde{y}, z)$, is constant in the $\tilde{x}$ direction perpendicular to the $(\tilde{y}, z)$ image plane. This is computationally less expensive than its 3D analogue, but yet appropriate for the present study. The applied procedure is similar to the approaches of Daily et al. (1992) and LaBrecque et al. (1996). Here, according to *Occam's razor* (plurality should not be postulated without necessity), regularisation is performed by seeking the 'smoothest' model subject to fitting the data. This is accomplished by formulating the inverse problem as an optimisation problem and incorporating the smoothness constraint within the associated objective function.

Let **m** denote the parameter vector, **d** the data vector, **W** a data weighting matrix (derived from data errors), and **f** the operator of the forward solution. The objective function to be minimised in the inversion then is

$$\Psi(\mathbf{m}) = \|\mathbf{W}[\mathbf{d} - \mathbf{f}(\mathbf{m})]\|^2 + \alpha\|\mathbf{Rm}\|^2, \tag{1}$$

where α is the so-called regularisation parameter, and **R** is a matrix evaluating the (first-order) roughness of **m**. Due to the typically wide magnitude range of earth conductivities and measured transfer resistances, we use log-transformed parameters and data in the inversion. Given a discrete pixel parameterisation $\{\sigma_{b,j} | j = 1, \ldots, M\}$ (S/m) of $\sigma_b(\tilde{y}, z)$ (Fig. 2) and a set of resistance data $\{r_i | i = 1, \ldots, N\}$ (V/A), **m** and **d** are defined as

$$m_j = \ln \sigma_{b,j}, \qquad d_i = \ln r_i, \tag{2}$$

where M and N are numbers of model parameters and measurements, respectively. Assuming uncorrelated data errors $\{\varepsilon_i\}$, the data weighting matrix takes the simple diagonal form

$$\mathbf{W} = \mathrm{diag}\{1/\varepsilon_1, \ldots, 1/\varepsilon_N\}. \tag{3}$$

The roughness vector **Rm** in Eq. (1) approximates the (2D) gradient of the continuous distribution $\sigma_b(\tilde{y}, z)$ associated with the discrete parameterisation **m** such

that

$$\|\mathbf{Rm}\|^2 \approx \int\int \|\nabla(\ln \sigma_b)\|^2 \, d\tilde{y} \, dz, \tag{4}$$

where the integration covers the $(\tilde{y}, z)$ image plane.

The 2D ERT forward problem, defining the operator $\mathbf{f}$ in Eq. (1), is given by the 1D Fourier transform of the Poisson equation for a 3D point source in the image plane at $(\tilde{y}_s, z_s)$ with current I (A):

$$\frac{\partial}{\partial \tilde{y}}\left(\sigma_b \frac{\partial \phi}{\partial \tilde{y}}\right) + \frac{\partial}{\partial z}\left(\sigma_b \frac{\partial \phi}{\partial z}\right) - k^2 \sigma_b \phi = -I\delta(\tilde{y} - \tilde{y}_s)\delta(z - z_s). \tag{5}$$

Herein, k (m^{-1}) is the wavenumber corresponding to the $\tilde{x}$ direction, ϕ (V) is the electric potential in the Fourier domain, and δ is the Dirac delta function. For given boundary conditions, Eq. (5) is solved for $\phi(\tilde{y}, z)$ by means of the finite-element (FE) method, where the discretisation is chosen such that each model cell $\sigma_{b,j}$ of the parameterisation is represented by a set of lumped finite elements. Once the transformed electric potential distribution is computed for each current injection position, inverse Fourier transform and appropriate superposition yields the transfer resistance of any desired electrode configuration. Kemna (2000) details the forward modelling, including derivation and solution of the FE equations, implementation of boundary conditions, and the procedure used for inverse Fourier transform.

Due to the nonlinearity of the problem, the minimisation of the objective function in Eq. (1) results in an iterative Gauss–Newton scheme, where at each step p the linear system of equations

$$(\mathbf{A}_p^T\mathbf{W}^T\mathbf{W}\mathbf{A}_p + \alpha\mathbf{R}^T\mathbf{R})\Delta\mathbf{m}_p = \mathbf{A}_p^T\mathbf{W}^T\mathbf{W}[\mathbf{d} - \mathbf{f}(\mathbf{m}_p)] - \alpha\mathbf{R}^T\mathbf{R}\mathbf{m}_p \tag{6}$$

is solved for a model update $\Delta\mathbf{m}_p$. In Eq. (6),

$$\mathbf{A}_p = \left.\frac{\partial \mathbf{f}}{\partial \mathbf{m}}\right|_{\mathbf{m}=\mathbf{m}_p} \tag{7}$$

is the sensitivity (Jacobian) matrix of the problem, evaluated at the current model $\mathbf{m}_p$. Eq. (6) is solved by means of the conjugate-gradient method, using a simple diagonal scaling for preconditioning. At each inverse iteration step, a univariate search is performed (deGroot-Hedlin and Constable, 1990) to find the maximum value of α (i.e. the spatially smoothest model) which locally minimises the data misfit, $\|\mathbf{W}[\mathbf{d} - \mathbf{f}(\mathbf{m})]\|^2$. Moreover, the optimum step length into the direction of $\Delta\mathbf{m}_p$ is determined by means of three-point parabolic interpolation (LaBrecque et al., 1996) to prevent the algorithm from overshooting. Numerical details are given in Kemna (2000).

As the starting model of the inversion we use a homogeneous model, determined from the mean measured response. The iteration process is stopped when the value of data misfit reaches the value 1. This implies that the data errors must be known a priori. We employ a constant error model (Binley et al., 1995). For the (background) field data, we considered a noise level of 20% in the measured resistances, i.e. we set $\varepsilon_i = 0.2$. This relatively high level accounts for systematic errors associated with the simple 2D representation of a real 3D distribution of σ_b.

There is some arbitrariness in the choice of the regularisation. In principle, regularisation can be accomplished with a view to purely numerical aspects (e.g. Levenberg–Marquardt technique), although we favour to constrain the inverse solution by imposing certain (unique) characteristics on the model, i.e. in some way account for the physical problem itself. However, there are still numerous possible approaches to do this and, hence, the question directly arises how the choice of the imposed model characteristics does influence the final inversion result. In order to assess the uncertainty in the reconstructed image associated with this arbitrariness, we considered three different types of model smoothing: isotropic, horizontally dominated, and vertically dominated smoothing. These types can be easily accomplished by separating the matrix $\mathbf{R}$ with respect to horizontal ($\tilde{y}$) and vertical (z) directions into matrices $\mathbf{R}_H$ and $\mathbf{R}_V$, respectively, and introducing two corresponding smoothing parameters α_H and α_V (Ellis and Oldenburg, 1994):

$$\mathbf{R}^T\mathbf{R} = \alpha_H\mathbf{R}_H^T\mathbf{R}_H + \alpha_V\mathbf{R}_V^T\mathbf{R}_V. \tag{8}$$

We studied the cases $\alpha_H/\alpha_V = 1$, $\alpha_H/\alpha_V = 10$, and $\alpha_H/\alpha_V = 0.1$, which we will simply refer to hereafter as isotropic, horizontal, and vertical smoothing, respectively.

3.2. ERT monitoring

When used for monitoring dynamic processes, the main objective of ERT is not necessarily to produce absolute images of electrical conductivity, but rather to map temporal changes thereof in the imaged plane (or space). At first glance, a change in $\mathbf{m}$ over time t (s) may be readily imaged by independently applying the above inversion scheme to two data sets $\mathbf{d}_0$ and $\mathbf{d}$, measured at times $t = 0$ and $t > 0$, respectively, and afterwards analysing the respective inversion results $\mathbf{m}_0$ and $\mathbf{m}$ in terms of $\mathbf{m} - \mathbf{m}_0$ (Ramirez et al., 1993). Unfortunately, with such an approach even small uncertainties in the individually inverted images, associated with uncertainties in the data and the method itself, may be enormously amplified in the difference image. This may not only lead to a significant reduction of (difference) image quality, but also to the formation of misleading artefacts. However, the problem can be avoided by directly formulating the inversion in terms of data residues and model perturbations associated with the given changes over time.

Daily et al. (1992) proposed to invert the ratios of measured transfer resistances at times $t > 0$ and $t = 0$ (background data) multiplied by the corresponding, calculated response for a homogeneous reference model. By this, temporal changes in the data are mapped into an absolute image which reflects the underlying conductivity changes in the subsurface (since the reference model is homogeneous). Recently, LaBrecque and Yang (2000) presented a generalisation of this procedure where the restriction of a homogeneous reference model is dropped. In their approach, which they refer to as 'difference inversion', the background model $\mathbf{m}_0$ itself serves as the reference, which is of course not necessarily homogeneous. The corresponding objective function to be minimised then is

$$\Psi_{\text{diff}}(\mathbf{m}) = \|\mathbf{W}[\mathbf{d} - \mathbf{d}_0 + \mathbf{f}(\mathbf{m}_0) - \mathbf{f}(\mathbf{m})]\|^2 + \alpha\|\mathbf{R}(\mathbf{m} - \mathbf{m}_0)\|^2. \tag{9}$$

Note that in Eq. (9), smoothness is directly imposed on the model change $\mathbf{m} - \mathbf{m}_0$. Minimisation of the objective function in Eq. (9) is accomplished analogous to the conventional 'absolute inversion' according to Eqs. (1) and (6).

As the starting model for the difference inverse iterations we use the background model $\mathbf{m}_0$, which is obtained by carrying out an absolute inversion (see Section 3.1) of the background data $\mathbf{d}_0$. The noise level in the resistance data with respect to temporal changes during the tracer experiment was estimated at about 3%, i.e. in the difference inversion we used $\varepsilon_i = 0.03$ (for both field and synthetic experiments). However, the overall difference inversion procedure, including choice and variation of the regularisation parameter, determination of the optimum step length, and the stopping criterion, is completely the same as described in Section 3.1.

3.3. ERT sensitivity

Spatial resolution is a critical but often neglected attribute of ERT imaging. Resolution is a complex function of numerous factors (e.g. electrode layout, measurement schedule, data quality, imaging algorithm, electrical conductivity distribution) and, in general, varies significantly across the image plane. One way to assess image resolution and its spatial variation is to explicitly compute the parameter resolution matrix of the corresponding inverse problem (Alumbaugh and Newman, 2000). Unfortunately, this approach is computationally quite expensive for large tomographic problems.

However, also a simple sensitivity analysis provides some valuable insight into the resolution problem (recall that, in ERT, sensitivity states how a local change in electrical conductivity affects a single transfer resistance measurement). The spatial sensitivity patterns of all individual measurements may be superimposed in absolute (squared) terms according to

$$\sum_{i=1}^{N}\left[\frac{(\mathbf{A})_{ij}}{\varepsilon_i}\right]^2 = (\mathbf{A}^{\mathrm{T}}\mathbf{W}^{\mathrm{T}}\mathbf{W}\mathbf{A})_{jj}, \tag{10}$$

in order to obtain a map indicating how the image plane is, analogous to ray-type tomography problems, 'covered' by the data (Kemna, 2000). Obviously a poorly covered region is unlikely to be well resolved. Fig. 3 shows such an accumulated sensitivity map as typical for the present ERT electrode arrangement and measurement schedule (the exemplary map corresponds to the reconstructed solute plume model at

deep position for a dispersion coefficient of 0.1 m^2/d Fig. 5(g)). The sensitivity variations across the image plane are evident. In principle, as to be expected and well-known (Ramirez et al., 1993), overall sensitivity decreases dramatically towards the bottom of the ERT plane, indicating significant loss of resolution in this region.

3.4. Relation between bulk electrical conductivity and tracer concentration

In order to relate tracer concentration to bulk electrical conductivity it is instructive to first recall some petrophysical fundamentals. With ERT, the (ohmic) bulk electrical conductivity of the aqueous and solid phase mixture, σ_b (S/m), is measured. The electrical conductivity of the aqueous solution filling the pore space, σ_w (S/m), and the (ohmic) surface conductivity, σ_s (S/m), both contribute to σ_b. In most models (Waxman and Smits, 1968), these contributions act in parallel, i.e.

$$\sigma_b = \frac{\sigma_w}{F} + \sigma_s, \tag{11}$$

with F being the formation factor accounting for the pore space geometry (porosity, tortuosity) according to Archie's law (Archie, 1942). Following the theoretical model of Johnson et al. (1986), the surface conductivity in Eq. (11) can be expressed as

$$\sigma_s = \frac{2\mu_s Q_s}{F\Lambda}, \tag{12}$$

where Λ (m) is an intrinsic measure of interconnected pore size, Q_s (C/m^2) is the surface charge density, and μ_s ($m^2/V/s$) is the effective ionic mobility in the electrical double layer around the charged surface. Since the chemical composition of the double layer depends on the composition of the aqueous phase, μ_s is a (generally nonlinear) function of σ_w. The pore-size parameter Λ accounts for different surface and bulk tortuosity factors. Eq. (12) is, in principle, identical with the bulk electrical conductivity models of Waxman and Smits (1968) and Rink and Schopper (1974).

During the field tracer experiment, multilevel groundwater samples were taken in the boreholes used for ERT and subsequently analysed for both Br^- concentration, C (g/m^3), and electrical conductivity.

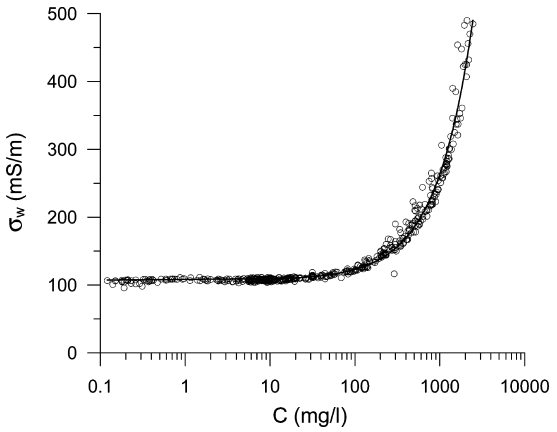

Fig. 4. Groundwater electrical conductivity versus Br^- concentration as measured for multilevel samples taken in the ERT boreholes during the tracer experiment (open circles). The solid curve represents the linear fit to the data (coefficient of determination $R^2 = 0.98$).

For the range of Br^- concentrations observed in this study, σ_w was found to be a linear function of C (Fig. 4):

$$\sigma_w - \sigma_{w,in} = \frac{C - C_{in}}{\gamma}, \tag{13}$$

where γ is a calibration constant (here $\gamma = 6.41$ (mg/l)/(mS/m)), and C_{in} and $\sigma_{w,in}$ are, respectively, background Br^- concentration (here $C_{in} = 0$) and background or initial electrical conductivity of the groundwater due to background salinity. The initial groundwater electrical conductivity can be assumed to be a constant (i.e. independent of location) when the background chemical composition of the groundwater is constant in space. In the Krauthausen aquifer, $\sigma_{w,in}$ was 107.4 mS/m during the tracer test (Fig. 4).

As already indicated above, σ_b is in general a nonlinear function of σ_w. In many cases, however, it may be fairly well approximated by a linear calibration function (Sen et al., 1988; Rhoades et al., 1989)

$$\sigma_b = a(\mathbf{x})\sigma_w + b(\mathbf{x}), \tag{14}$$

where $a(\mathbf{x})$ and $b(\mathbf{x})$ are empirical calibration parameters independent of salinity. Recently, Revil and Glover (1998) found, for shaly sands, that the specific surface conductance ($\mu_s Q_s$) is nearly constant

for varying σ_w in the range $\sigma_w > 100$ mS/m. By comparing Eq. (14) with Eqs. (11) and (12), we may therefore assume in our case ($\sigma_{w,in} = 107.4$ mS/m) that the parameter $a(\mathbf{x})$ depends predominantly on the formation factor F, i.e. on porosity and bulk tortuosity, whereas $b(\mathbf{x})$ is determined by both bulk and surface geometric parameters (F, Λ) as well as μ_s and Q_s. However, in a heterogeneous aquifer the calibration parameters obviously depend on location $\mathbf{x}$. This fact is also clearly reflected by the reconstructed distribution of initial bulk electrical conductivity, $\sigma_{b,in}(\tilde{y}, z)$, which varies considerably with location despite the relative constant $\sigma_{w,in}$ (Fig. 7). Since it is impossible to identify a calibration relation at each location, we need to make some assumptions about the spatial variability of $a(\mathbf{x})$ and $b(\mathbf{x})$.

In a first working hypothesis, we assume that the slope of the calibration relation, $a(\mathbf{x})$, is invariant with location. This assumption comes down to assuming a constant formation factor F. Then, from Eqs. (13) and (14), the relation between the absolute temporal changes in $\sigma_b(\mathbf{x};t)$ and $\sigma_w(\mathbf{x};t)$ or $C(\mathbf{x};t)$ at a certain location $\mathbf{x}$ becomes independent of location:

$$\Delta_a\sigma_b(\mathbf{x};t) := \sigma_b(\mathbf{x};t) - \sigma_{b,in}(\mathbf{x}) = \frac{C(\mathbf{x};t) - C_{in}}{\gamma/a}. \tag{15}$$

Eq. (15) states that the (absolute) concentration change at a location $\mathbf{x}$, $C(\mathbf{x};t) - C_{in}$, can be derived from the absolute change in bulk electrical conductivity.

In a second working assumption, we assume that the ratio $b(\mathbf{x})/a(\mathbf{x})$ is spatially constant. According to the above equations (Eqs. (11), (12), and (14)), this assumption comes down to assuming a constant $\mu_s Q_s/\Lambda$. However, when the product $a(\mathbf{x})\sigma_w$ is considerably larger than $b(\mathbf{x})$ (high-salinity limit), a violation of this assumption does not have an important impact. Then, the relation between the relative temporal changes in $\sigma_b(\mathbf{x};t)$ and $\sigma_w(\mathbf{x};t)$ or $C(\mathbf{x};t)$ becomes independent of $\mathbf{x}$:

$$\Delta_r\sigma_b(\mathbf{x};t) := \frac{\sigma_b(\mathbf{x},t)}{\sigma_{b,in}(\mathbf{x})} - 1 = \frac{C(\mathbf{x},t) - C_{in}}{\gamma(\sigma_{w,in} + b/a)}. \tag{16}$$

Following Eq. (16), the concentration change at $\mathbf{x}$ can be derived from the relative change in bulk electrical conductivity using a location-independent calibration relation.

In the derivation of Eqs. (15) and (16), we took for granted that changes in bulk electrical conductivity due to temperature effects can be neglected. However, given the fact that the groundwater temperature, T (°C), varied only slightly during the time period analysed in this study ($\Delta T < 1$ °C) and recalling that (Sen and Goode, 1992)

$$\Delta_r\sigma_w(T) := \frac{\sigma_w(T)}{\sigma_w(T_0)} - 1 = \kappa(T)(T - T_0), \tag{17}$$

with $\kappa(T) \approx 0.025\ °C^{-1}$ for the observed temperatures around $T_0 \approx 13$ °C, this assumption is justified to an acceptable degree.

3.5. Transport modelling

3D solute transport in porous media is described by the convection–dispersion equation (CDE)

$$\theta\frac{\partial C}{\partial t} = -\mathbf{q}\cdot\nabla C + \nabla\cdot(\theta\mathbf{D}_d\nabla C), \tag{18}$$

where θ is the water-filled porosity, $\mathbf{q}$ (m/s) is the Darcy flux vector, $\mathbf{D}_d$ (m^2/s) is the local-scale dispersion tensor, and C (g/m^3) is the solute concentration. For steady-state water flow in a heterogeneous aquifer, both $\mathbf{q}$ and $\mathbf{D}_d$ vary with location, i.e. are functions of $\mathbf{x}$.

In an equivalent homogeneous medium and for a mean flow in the horizontal direction, the equivalent CDE is written as

$$\frac{\partial C}{\partial t} = -v_{x'}\frac{\partial C}{\partial x'} + D_L\frac{\partial^2 C}{\partial x'^2} + D_{TH}\frac{\partial^2 C}{\partial y'^2} + D_{TV}\frac{\partial^2 C}{\partial z'^2}, \tag{19}$$

where x', y', and z' are the coordinates in the direction of the mean flow, perpendicular to the mean flow in the horizontal direction, and perpendicular to the mean flow in the vertical direction, respectively, $v_{x'}$ (m/s) is the pore water velocity, D_L (m^2/s) the longitudinal dispersion, D_{TH} (m^2/s) the transverse dispersion in the horizontal direction, and D_{TV} (m^2/s) the transverse dispersion in the vertical direction. Since a horizontal mean flow is considered, only the horizontal coordinate axes were rotated so that the x' coordinate axis corresponds with the mean flow direction (Fig. 1). The vertical axis was translated

by an offset Δz ($z' = z - \Delta z$) in order to account for the vertical subsidence of the tracer plume until crossing the ERT image plane due to density differences. Neglecting molecular diffusion, the dispersion coefficients can be written as

$$D_{\mathrm{L}} = \lambda_{\mathrm{L}} v_{x'}, \qquad D_{\mathrm{TH}} = \lambda_{\mathrm{TH}} v_{x'}, \qquad D_{\mathrm{TV}} = \lambda_{\mathrm{TV}} v_{x'}, \tag{20}$$

where λ_{L}, λ_{TH}, and λ_{TV} (m) are the longitudinal, transverse horizontal, and transverse vertical dispersivities. For an initial concentration C_0 inside a parallelepiped of vertical extension $2L_{z'}$ and lateral extension $2L_{x'} = 2L_{y'}$, oriented to the mean flow direction, and an initial concentration C_{in} outside the parallelepiped, the analytical solution of Eq. (19) in an infinite medium is

$$\begin{aligned} c(x', y', z', t) &= \frac{1}{8}\left[\operatorname{erf}\left(\frac{x' + L_{x'} - v_{x'}t}{\sqrt{4 v_{x'} \lambda_{\mathrm{L}} t}}\right) - \operatorname{erf}\left(\frac{x' - L_{x'} - v_{x'}t}{\sqrt{4 v_{x'} \lambda_{\mathrm{L}} t}}\right)\right] \\ &\times\left[\operatorname{erf}\left(\frac{y' + L_{y'}}{\sqrt{4 v_{x'} \lambda_{\mathrm{TH}} t}}\right) - \operatorname{erf}\left(\frac{y' - L_{y'}}{\sqrt{4 v_{x'} \lambda_{\mathrm{TH}} t}}\right)\right] \\ &\times\left[\operatorname{erf}\left(\frac{z' + L_{z'}}{\sqrt{4 v_{x'} \lambda_{\mathrm{TV}} t}}\right) - \operatorname{erf}\left(\frac{z' - L_{z'}}{\sqrt{4 v_{x'} \lambda_{\mathrm{TV}} t}}\right)\right], \end{aligned} \tag{21}$$

where c is the relative concentration $(C - C_{\mathrm{in}})/(C_0 - C_{\mathrm{in}})$, and the origin of the coordinate system is assumed to coincide with the centre of the parallelepiped. In association with the field experiment, the vertical and lateral extensions are defined as $2L_{z'} = 1$ m (filtered section of the injection well) and $2L_{x'} = 2L_{y'} = 2.77$ m. The latter value was calculated from the volume of injected tracer solution (2000 l) and the mean aquifer porosity (26%) according to earlier sample analyses (Vereecken et al., 2000).

Eq. (21) can also be written in terms of $\Delta_{\mathrm{a}}\sigma_{\mathrm{b}}$ (Eq. (15)) or $\Delta_{\mathrm{r}}\sigma_{\mathrm{b}}$ (Eq. (16)) by multiplying it by a factor, respectively, $M_{0\mathrm{a}}$ or $M_{0\mathrm{r}}$:

$$\begin{aligned} M_{0\mathrm{a}} &= \Delta_{\mathrm{a}}\sigma_{\mathrm{b}0} = \frac{C_0 - C_{\mathrm{in}}}{\gamma/a}, \\ M_{0\mathrm{r}} &= \Delta_{\mathrm{r}}\sigma_{\mathrm{b}0} = \frac{C_0 - C_{\mathrm{in}}}{\gamma(\sigma_{\mathrm{w,in}} + b/a)}. \end{aligned} \tag{22}$$

The factors $M_{0\mathrm{a}}$ and $M_{0\mathrm{r}}$ correspond to, respectively, absolute and relative change in bulk electrical conductivity when the Br^- concentration of the pore water equals C_0.

The parameters λ_{L}, λ_{TH}, λ_{TV}, $v_{x'}$, the factors $M_{0\mathrm{a}}$ or $M_{0\mathrm{r}}$, the angle β between the x and x' (or y and y') coordinate axes, and the vertical offset Δz are obtained from a least-squares fit of Eq. (21) to the ERT-derived distributions $\Delta_{\mathrm{a}}\sigma_{\mathrm{b}}(\tilde{y}, z)$ or $\Delta_{\mathrm{r}}\sigma_{\mathrm{b}}(\tilde{y}, z)$. The NLIN procedure of the SAS software package (SAS Institute Inc., 1989) was used for the nonlinear least-squares optimisation.

In Eq. (19), the transport of the entire solute plume is described assuming an equivalent homogeneous medium. However, for large solute plumes compared with the scale of heterogeneity of local hydraulic properties, the solute plume is distorted by spatial variations of advection velocities. Although the spreading of the plume, which is quantified by centralised second spatial moments, may be described by an equivalent CDE, the local-scale concentrations or the concentration distribution within the plume might be poorly described by the equivalent CDE (Eq. (19)). Rather than considering a 3D transport process in an equivalent homogeneous medium, the medium can be conceptualised as a set of independent stream tubes parallel to the mean flow direction x' (Simmons, 1982). In the latter approach, each pixel in the ERT image plane is associated with an individual stream tube crossing the image plane at the pixel's location $(\tilde{y}, z)$. Transport in each stream tube is described by an equivalent 1D CDM

$$\frac{\partial C}{\partial t} = -v_{\mathrm{s}}(\tilde{y}, z)\frac{\partial C}{\partial x'} + v_{\mathrm{s}}(\tilde{y}, z)\lambda_{\mathrm{s}}(\tilde{y}, z)\frac{\partial^2 C}{\partial x'^2}, \tag{23}$$

where $v_{\mathrm{s}}(\tilde{y}, z)$ is the advection velocity and $\lambda_{\mathrm{s}}(\tilde{y}, z)$ the longitudinal dispersivity in the stream tube. The variability of v_{s} across the ERT plane is a measure of plume distortion due to spatial variations in water flux in the aquifer. The average value of λ_{s} is a measure of the dilution of the locally observed

concentrations due to mixing of the injected tracer solution with groundwater. Due to distortion of the injected solute plume by spatial variations in advection velocity, the effective area across which dispersive mixing can take place is larger in a heterogeneous than in a homogeneous flow field (Vanderborght, 2001). Therefore, $\lambda_s > \lambda_{dL}$, where λ_{dL} is the local-scale longitudinal dispersivity. On the other hand, the distortion process is generally faster than the mixing process so that $\lambda_s < \lambda_L$ at relatively small times after the injection. The relation between the spatial variability of the hydraulic conductivity and the local-scale dispersion on one hand and λ_s on the other is discussed by Vanderborght and Vereecken (2002).

For each pixel in the ERT plane where a significant amount of Br^- was observed, the solution of Eq. (23) was fitted to the locally observed time series or breakthrough curve (BTC) of relative bulk electrical conductivity changes

$$\Delta_r\sigma_b(x',t) = \frac{M_{0s}}{2}\left[\mathrm{erf}\left(\frac{x' + L_{x'} - v_s t}{\sqrt{4v_s\lambda_s t}}\right) - \mathrm{erf}\left(\frac{x' - L_{x'} - v_s t}{\sqrt{4v_s\lambda_s t}}\right)\right], \quad (24)$$

where M_{0s} is a fitting factor. For large injection surfaces and at the centre of the plume, M_{0s} converges to M_{0r}. However, due to lateral mixing and solute mass transfer to stream tubes that do not cross the initial injection volume, M_{0s} is smaller than M_{0r}. The x' coordinate of each pixel in the ERT plane was calculated from the pixel location $\mathbf{x}$ and the angle β that was obtained from the fit of the 3D equivalent transport model (Eq. (21)).

4. Results

4.1. Synthetic experiment

The numerical experiments were conducted to assess the ERT resolution, quantified in terms of recovered dispersion coefficients, for the electrode setup and measurement schedule as used in the field experiment. The synthetic solute plume model distributions of relative bulk electrical conductivity changes, $\Delta_r\sigma_b$, the reconstructed distributions of $\Delta_r\sigma_b$ using an isotropic smoothing for regularisation in the ERT inversion, and the fitted diffusion models to the reconstructed $\Delta_r\sigma_b$ are shown in Fig. 5. The centre position distributions are reasonably well recovered. The low sensitivity of ERT measurements to local bulk electrical resistivity changes at the bottom of the ERT plane (Fig. 3) visibly influences the quality of the inverted distributions. The contrast in the reconstructed deep position distributions is somewhat lower than in the premised (input model) distributions. The lower contrast goes along with a larger spreading or smoothing of the reconstructed than the premised distributions. Despite the lower contrast, the solute 'mass' in the recovered deep position distributions, which was determined from the diffusion model fit, is slightly larger than the mass in the premised distributions (108%). For the centre position distributions, the average of the fitted mass in the reconstructed distributions is 98% of the premised mass.

The effect of smoothing is quantified in terms of recovered dispersion coefficients, which are plotted versus the premised ones in Fig. 6. All fitted dispersion coefficients are larger than the premised ones, which reveals the smoothing effect of the imaging algorithm due to the imposed regularisation. Smoothing seems to be more critical outside the sensitive region of the ERT image plane, i.e. for the deep position distributions. The fitted vertical dispersion coefficients are in general quite close to the premised ones. They are, in the sensitive region (centre position), a factor 1.0–1.4 and, in the less sensitive region (deep position), a factor 1.1–5.7 larger than the premised ones, with the largest discrepancy occurring for the smallest coefficient under consideration. The fitted horizontal dispersion coefficients deviate more from the premised ones: by a factor 1.4–2.2 in the sensitive region and by a factor 2.3–6.8 in the less sensitive region. Although an isotropic smoothing was employed for the regularisation, the inverted distributions are apparently more smoothed in the horizontal than in the vertical direction and, thus, an anisotropic diffusion process is suggested by the reconstructed distributions.

The effect of using anisotropic smoothing for regularisation in the ERT imaging algorithm was also

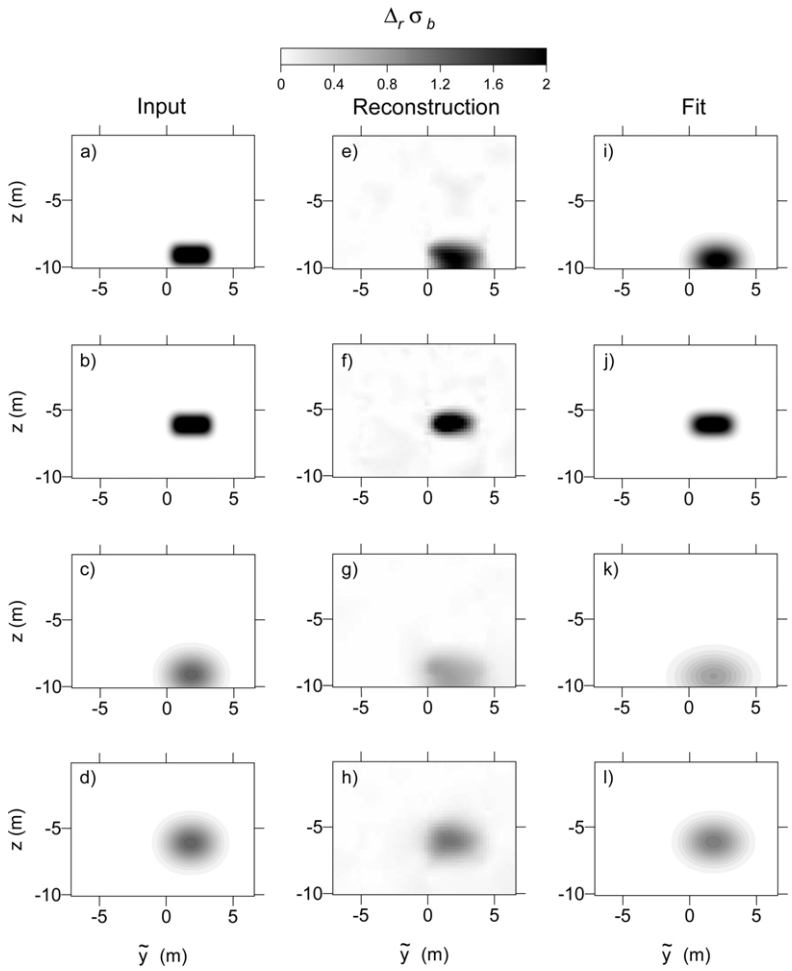

Fig. 5. Synthetic solute plume distributions of relative bulk electrical conductivity changes, $\Delta_r\sigma_b$, generated by a diffusion model (panels (a)–(d)); reconstructed distributions from synthetic, noisy ERT data that were calculated from the generated distributions (panels (e)–(h)); and fit of the diffusion model to the reconstructed distributions (panels (i)–(l)). An isotropic smoothing was used to regularise the ERT inversion. Distributions in panels (a) and (b) correspond to a dispersion coefficient $D = 0.01\ \mathrm{m}^2/\mathrm{d}$ and distributions in panels (c) and (d) to a dispersion coefficient $D = 0.1\ \mathrm{m}^2/\mathrm{d}$. Distributions in panels (a) and (c) are the deep position distributions and in panels (b) and (d) the centre position distributions.

quantified in terms of recovered dispersion coefficients. The corresponding results are listed in Table 1. As to be expected, imposing horizontal smoothing for the regularisation leads to increased horizontal and decreased vertical fitted dispersion coefficients compared to the results using isotropic smoothing, and vice versa for vertical smoothing. Again, the impact of the smoothing anisotropy is larger in the less sensitive region of the ERT plane. For the three considered regularisation methods, the fitted horizontal dispersion coefficients overestimate the premised one and the differences among the recovered values are smaller than the deviations from the premised one. On the other hand, the recovered vertical dispersion coefficients are smaller (horizontal smoothing) or larger (isotropic and vertical smoothing) than the premised value and the best estimate is obtained for the centre position model using isotropic smoothing.

We conclude that the relatively large horizontal (cross-hole) separation of the borehole electrodes compared with their vertical (in-hole) separation leads to a smaller spatial resolution in the horizontal than in

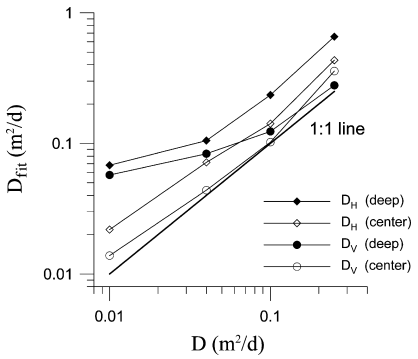

Fig. 6. Fitted horizontal, D_H, and vertical, D_V, dispersion coefficients to reconstructed solute plumes versus the premised dispersion coefficients for the centre position and deep position distributions (Fig. 5). The reconstructed distributions were obtained using an isotropic smoothing for regularisation in the ERT inversion.

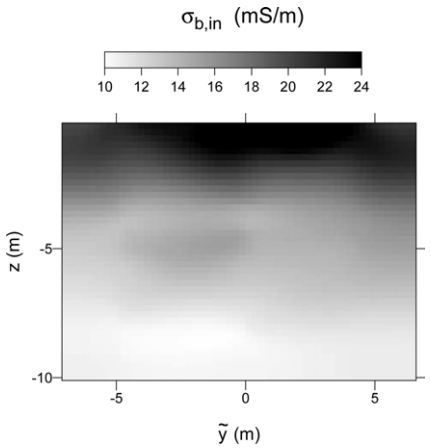

Fig. 7. ERT background image exhibiting the initial distribution of bulk electrical conductivity, $\sigma_{b,in}$, before tracer injection. Isotropic smoothing was used for regularisation in the inversion.

the vertical direction in the region of interest. Yet, the resolution of the ERT imaging procedure is not constant over the entire image plane and relatively high horizontal and vertical resolution is obtained in the sensitive (centre) region of the ERT plane.

4.2. Observed tracer breakthrough in the ERT image plane

By successively applying the difference inversion scheme (Section 3.2) to the ERT data sets measured at selected time intervals during the field tracer experiment, temporal changes in bulk electrical conductivity are imaged with reference to the background distribution $\sigma_{b,in}(\tilde{y}, z)$. The background distribution, as observed on day 0 just before tracer injection, was calculated using the absolute inversion scheme (Section 3.1) and is shown in Fig. 7. In principle, the recovered distribution reflects the lithological setting at the site (Fig. 2). The top loess layer is represented as a relatively conductive feature due to an increased clay content. Underneath in the saturated zone, bulk conductivity decreases continuously with depth, indicating a higher degree of compaction, and thus a larger formation factor (or smaller porosity), and/or a lower clay mineral content at greater depths. Furthermore, subtle vertical variations over the aquifer suggest an alternation of sand/gravel units with slightly different lithology, as confirmed by previous drillings (Fig. 2).

In Fig. 8, the temporal evolution of the relative bulk electrical conductivity change averaged over the ERT image plane, $\bar{\bar{\Delta}}_r\sigma_b(t)$, is shown together with the equivalent CDE model fit. The underlying distributions $\Delta_r\sigma_b(\tilde{y}, z)$ at the selected time intervals were derived from the ERT data using isotropic smoothing for regularisation in the inversion. The time series is relatively well described by the equivalent CDE. For larger times, $\bar{\bar{\Delta}}_r\sigma_b(t)$ values obtained from the average process become negative. This might have different reasons. First, averaging was performed over the entire image plane including the unsaturated top soil zone. Here, temporal moisture content changes associated with sporadic rainfall events during the

Table 1
Fitted horizontal, D_H, and vertical, D_V, dispersion coefficients to reconstructed solute plumes using three different types of regularisation: horizontal, isotropic, and vertical smoothing. The input plume models, one centred at 9.105 m (deep position, see Fig. 5(c)) and one at 6.105 m (centre position, see Fig. 5(d)) below surface, were generated assuming an isotropic diffusion process corresponding to a dispersion coefficient of 0.1 m^2/d

Position of plume	Smoothing	D_H (m^2/d)	D_V (m^2/d)
Centre	Horizontal	0.15	0.08
Centre	Isotropic	0.14	0.10
Centre	Vertical	0.13	0.11
Deep	Horizontal	0.28	0.09
Deep	Isotropic	0.24	0.12
Deep	Vertical	0.19	0.15

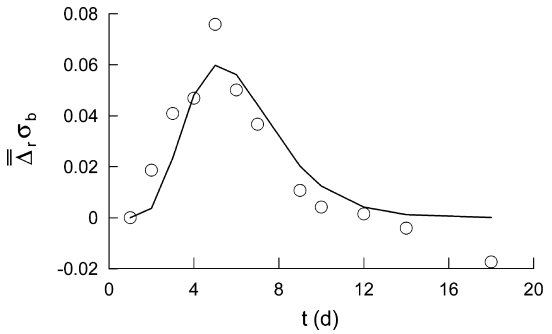

Fig. 8. Breakthrough curve of relative bulk electrical conductivity change averaged over the ERT image plane, $\bar{\bar{\Delta}}_r\sigma_b(t)$. Open circles indicate measured values, solid curve corresponds with the CDE model fit.

observation time are likely and could have caused the observed effect. However, the negative $\bar{\bar{\Delta}}_r\sigma_b(t)$ values could also indicate that at these times, the average ERT signature is not distinguishable from background noise, or that negative $\Delta_r\sigma_b$ values, the occurrence of which represents an artefact resulting from the regularisation used in the inversion, are at least of the same order of magnitude as the positive signature being of interest.

The spatial distribution of $\Delta_r\sigma_b$ in the ERT image plane, which was obtained using isotropic smoothing in the inversion, is shown for selected days after tracer injection in Fig. 9 together with the fitted $\Delta_r\sigma_b$ by the CDE (Eq. (21)). Also shown in Fig. 9 are horizontal and vertical profiles of, respectively, vertically and horizontally averaged $\Delta_r\sigma_b$. The equivalent CDE describes the general features of the recovered spatial distribution of $\Delta_r\sigma_b$ relatively well. The lateral spreading of the plume, which is observed across the ERT image plane, is more pronounced in the horizontal than in the vertical direction. The slightly smaller horizontal concentration gradients at the left-hand side of the CDE fitted plume result from the different angle between the mean flow direction and, respectively, the left and right-hand side of the ERT plane. At larger times (days 9 and 12), the location of the plume can still be seen in the ERT images but the inversion procedure generates negative $\Delta_r\sigma_b$ values around the plume that are of the same order of magnitude as the positive $\Delta_r\sigma_b$ values that mark the plume. From our experience, this is an effect of the smoothness constraint used for regularisation becoming evident for weak signal to noise ratios.

The effect of the type of smoothing that is used for regularisation in the ERT inversion is shown in Fig. 10, which shows inverted images of $\Delta_r\sigma_b$ at 5 days after tracer injection. Although the three distributions are equivalent in terms of data misfit, the shape of the recovered plume clearly depends on the type of smoothing (i.e. horizontal, isotropic, or vertical) used for the regularisation. Furthermore, like for the numerical experiment, it is evident that the regularisation procedure also influences the CDE fits and the fitted transport parameters (Table 2). Especially the transverse dispersivity in the vertical, λ_{TV}, and horizontal, λ_{TH}, directions are relatively strongly influenced by the regularisation procedure. For the horizontal smoothing, λ_{TV} is about a factor 2 smaller than for vertical smoothing, and vice versa for λ_{TH}. However, this apparently large variation is not so important when compared with the uncertainty and bias of parameter estimates due to the low sensitivity of the ERT method at the location where the breakthrough of the plume was observed (Fig. 6). The longitudinal dispersivity, λ_L, the advection velocity v, the angle β between the mean flow direction and the x-axis, and the factor M_{0r} are clearly less dependent on the applied type of smoothing. In other words, estimates of these parameters are rather insensitive to the arbitrariness associated with the choice of regularisation in the ERT imaging. Note, however, that the recovered λ_L values are likely to be overestimated to some degree due to the fact that we applied a simple 2D imaging approach to monitor a 3D process. Because of the diffuse character of electric fields, the tracer plume may still produce a signature in the 2D image plane though actually being located before or behind the plane. This obviously leads to an apparently earlier arrival and, in turn, later vanishing of the plume in the image plane.

The effect of the postulated relation between bulk electrical conductivity and Br^- concentration (Eqs. (15) vs. (16)) is shown in Fig. 11, which shows recovered images of $\Delta_r\sigma_b$ and $\Delta_a\sigma_b$ at 5 days after tracer injection. The range of the $\Delta_r\sigma_b$ colour scale is related to the range of the $\Delta_a\sigma_b$ colour scale as M_{0r} to M_{0a}. In the upper part of the ERT image plane (above -6 m) where hardly Br^- breakthrough was observed (Fig. 9), the variability of $\Delta_a\sigma_b$ is visibly larger than that of $\Delta_r\sigma_b$. The smaller variability of $\Delta_r\sigma_b$ results in part from the regularisation that constrains relative

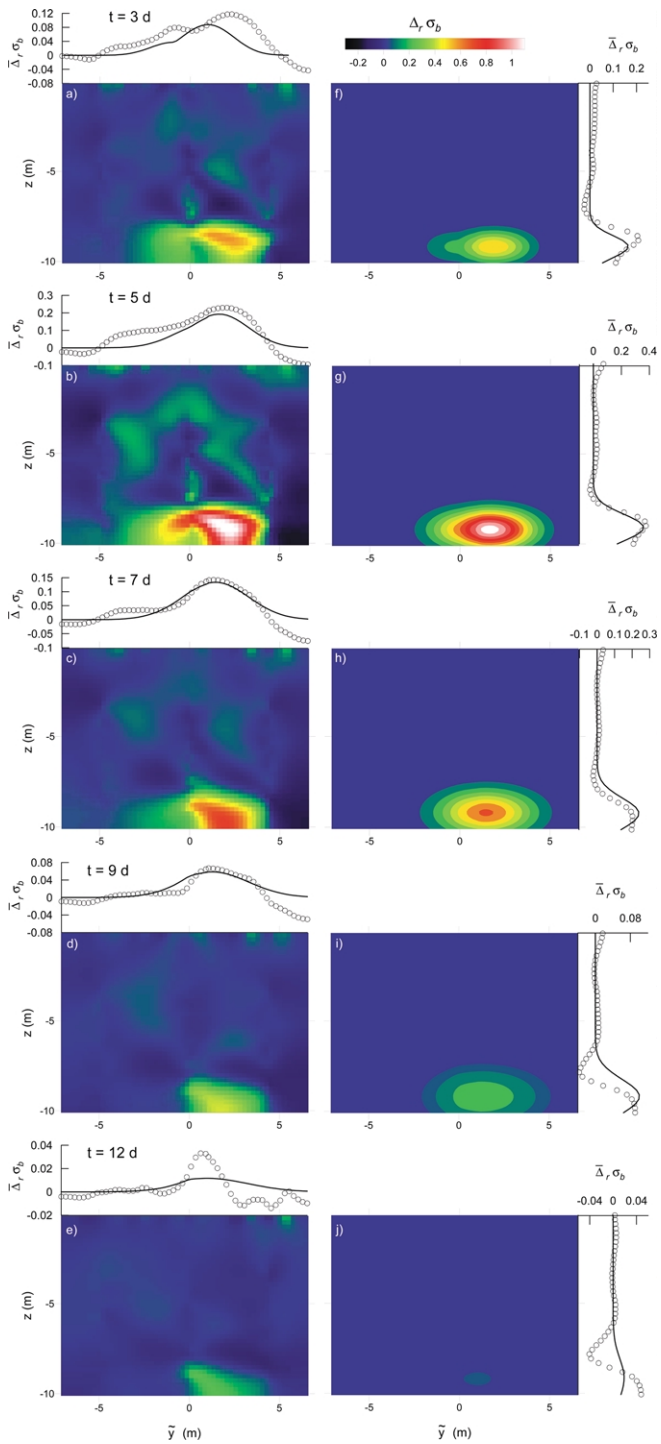

Fig. 9. Recovered spatial distribution of relative bulk electrical conductivity changes, $\Delta_r\sigma_b$, in the ERT image plane at 3, 5, 7, 9, and 12 days after tracer injection. Panels (a)–(e) are the ERT inversion results using isotropic smoothing for regularisation. Panels (f)–(j) are the fits of the equivalent CDE model (Eq. (21)). The plots above and on the right of the panels are profiles of, respectively, vertically and horizontally averaged bulk electrical conductivity changes, $\bar{\Delta}_r\sigma_b$. Open circles indicate ERT-derived values and solid curves CDE model fits.

electrical conductivity changes (strictly speaking it constrains absolute changes in log conductivity, see Eq. (4)). The absolute conductivity changes were calculated after the inversion from the relative concentration changes. On the other hand, the variability of $\Delta_a\sigma_b$ may also be attributed to small temporal variations in the background salinity or measurement noise, in combination with a larger slope $a(\mathbf{x})$ of the relation between σ_b and σ_w (Eq. (14)) in the upper than in the lower part of the ERT plane. The initial bulk electrical conductivity, $\sigma_{b,in}$, was larger in the upper part of the ERT plane (Fig. 7), which suggests a larger slope $a(\mathbf{x})$ and/or a larger intercept $b(\mathbf{x})$ in the upper part.

4.3. Discussion of fitted equivalent transport parameters

The larger extent of the plume in the lateral horizontal direction than in the vertical direction is reflected in larger λ_{TH} than λ_{TV} (Table 2). As discussed for the numerical experiment, ERT imaging results may suggest an apparent anisotropy in the dispersion process which could, in part, explain the difference between the fitted λ_{TH} and λ_{TV}. Since the fitted velocity is about 1 m/d (Table 2), the obtained dispersivities can be directly compared with the dispersion coefficients in Fig. 6 that were considered in the numerical experiment ($D = \lambda v$). According to the results from the synthetic study for the deep position (observed) distribution, a fitted λ_{TH} of 0.2 m would approximately correspond with an actual λ_{TH} of 0.1 m. The smallest fitted λ_{TV} in the numerical experiment for the deep position distribution was 0.06 m (corresponding with a premised value of 0.01 m, see Fig. 6). Therefore the obtained λ_{TV} from the field experiment, 0.05 m, would, according to the synthetic experiment, correspond with an actual λ_{TV} which is smaller than 0.01 m.

Table 2
Fitted parameters of the equivalent CDE (Eq. (21))

Input data	$\Delta_r\sigma_b$			$\Delta_a\sigma_b$
Smoothing	Horizontal	Isotropic	Vertical	isotropic
λ_L (m)	0.43	0.36	0.35	0.36
λ_{TH} (m)	0.28	0.19	0.16	0.18
λ_{TV} (m)	0.032	0.047	0.064	0.048
v (m/d)	0.82	0.98	1.06	0.98
β (deg)	5.7	6.9	8.0	7.4
Δz (m)	−1.64	−1.70	−1.81	−1.70
M_{0r} (−)	5.92	6.20	6.95	
M_{0a} (mS/m)				66

The larger λ_{TH} than λ_{TV} is not in agreement with theoretical (Dagan, 1988) and numerical studies (Naff et al., 1998) of 3D solute transport in heterogeneous hydraulic conductivity fields with an anisotropic structure. These studies suggest that λ_{TV} is similar or even larger than λ_{TH}. Because of the smaller vertical than horizontal extent of low hydraulic conductivity zones in an anisotropic medium, streamlines or particle trajectories bypass low conductivity zones more easily by vertical than by horizontal deviations. On the other hand, larger λ_{TH} than λ_{TV} were also observed in the Borden (Freyberg, 1986), Cape Cod (Garabedian et al., 1991), and a sandy aquifer in Denmark (Jensen et al., 1993). Dagan (1989) postulated that the larger horizontal than vertical lateral spreading of the plume might result from thin horizontal clay layers that impede vertical flow and force larger horizontal deviations of streamlines in order to bypass low hydraulic conductivity zones. At the Krauthausen test site, the vertical spreading of the plume might be impeded by the layer at the bottom of the aquifer (at about −10 m). Jensen et al. (1993) also reported a slightly larger lateral horizontal spreading of a chloride plume that sank to the impervious clay layer at the bottom of the aquifer than of a tritium plume that did not sink.

The fitted horizontal lateral dispersivity is about half the longitudinal dispersivity, λ_L. This ratio is relatively large compared with λ_{TH}/λ_L ratios reported for other tracer tests. The large λ_{TH}/λ_L ratio can be explained by the relatively small travel distance, 5.6 m. For larger travel distances, the longitudinal extension of the plume continues to increase whereas the lateral extension reaches a more or less constant value. As a consequence, the ratio λ_{TH}/λ_L is likely to decrease with increasing travel distance or with time since the dispersivity is a measure of the increase of spreading with time.

The longitudinal dispersivity, λ_L, obtained from this tracer test is about a factor 10–30 smaller than the equivalent longitudinal dispersivities that were derived from averaged BTCs of Br^- on reference planes or from spatial moments of the Br^- plume that

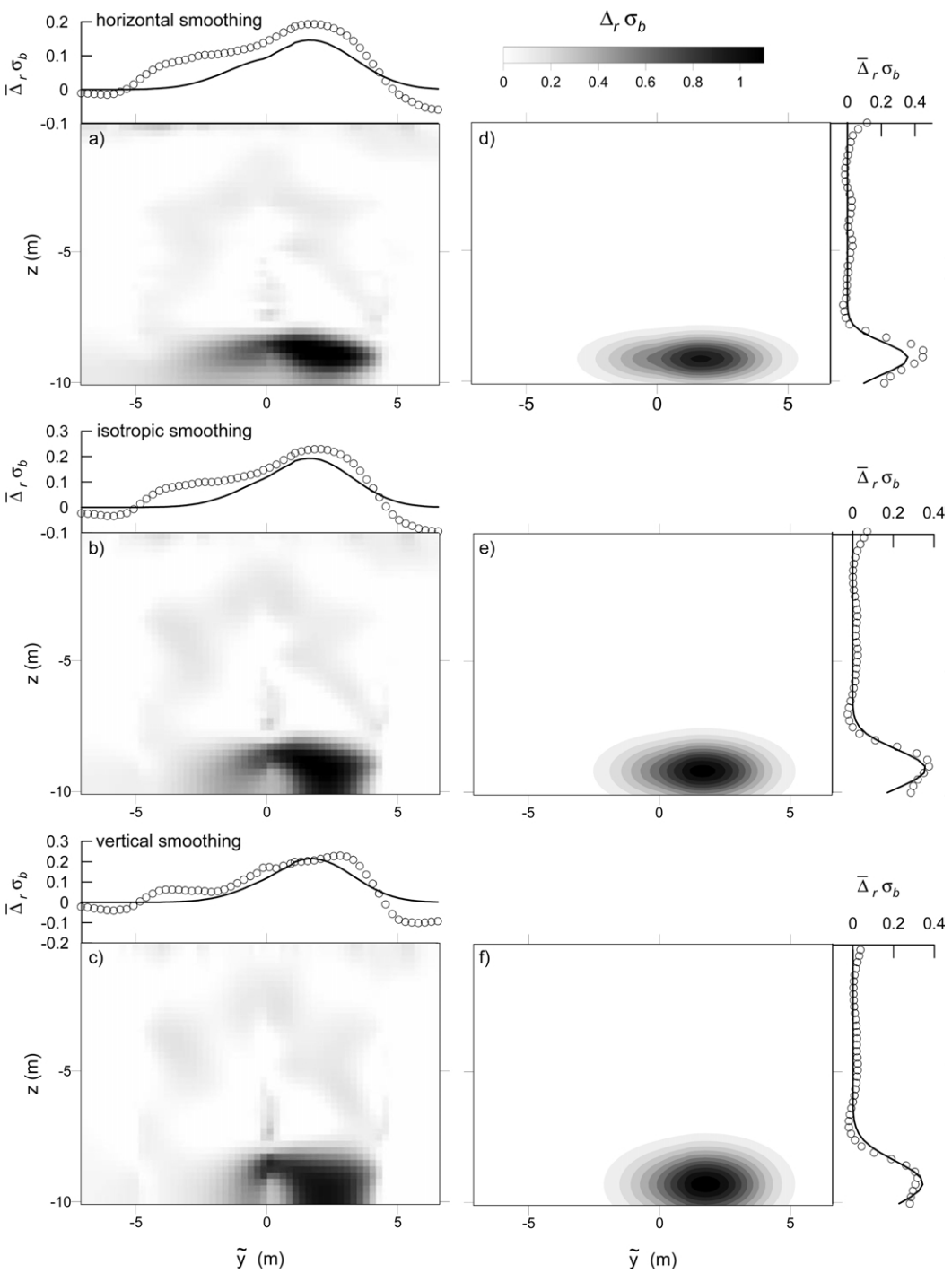

Fig. 10. Effect of different types of smoothing used for regularisation in the ERT inversion on the recovered distribution of relative bulk electrical conductivity changes, $\Delta_r\sigma_b$, (panels (a)–(c)) and on the corresponding CDE model fits (panels (d)–(f)). Distribution of $\Delta_r\sigma_b$ at 5 days after tracer injection is shown.

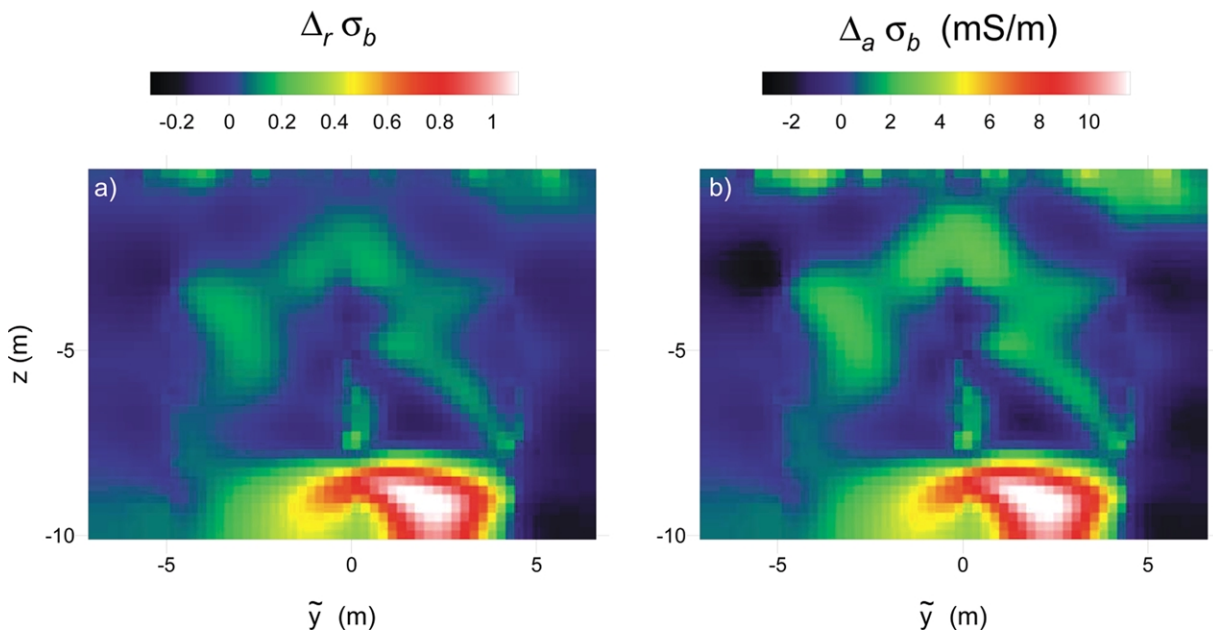

Fig. 11. Recovered spatial distribution of relative, $\Delta_r\sigma_b$, (panel (a)) and absolute, $\Delta_a\sigma_b$, (panel (b)), bulk electrical conductivity changes at 5 days after tracer injection. Isotropic smoothing was used for regularisation in the ERT inversion.

were observed during a previous tracer experiment (Vereecken et al., 2000; Vanderborght and Vereecken, 2001). Yet, comparing the relative small travel distance and lateral extent of the injection volume (relative to the correlation scale of hydraulic conductivity: 6.7 m in the horizontal direction and 0.4–0.6 m in the vertical direction, Vereecken et al., 2000) in this tracer test with those in the previous test, the smaller λ_L in this test is in agreement with what would be expected for a heterogeneous medium. The relatively small lateral extent of the injection volume also explains why the observed plume in the ERT image plane can be represented fairly well by a solute plume in an equivalent homogeneous medium. The heterogeneity of solute transport within the plume is represented by the variability of equivalent stream-tube velocities, v_s, and dispersivities, λ_s, which were derived from BTCs in individual pixels of the ERT plane. The average value and standard deviation of v_s and λ_s in a set of pixels is given in Table 3. To interpret the variability of v_s and λ_s among the pixels, also the average uncertainty of the v_s and λ_s estimates from a BTC in a single pixel is given in Table 3. The statistics listed in Table 3 are for the set of pixels where the uncertainty or coefficient of variation of λ_s was smaller than 0.4. Fig. 12 gives an impression of the spatial distribution of v_s and λ_s across the ERT plane. The relatively small variability of v_s and the agreement between the 'local-scale' equivalent dispersivity λ_s and 'plume-scale' equivalent dispersivity λ_L indicate that transport is relatively uniform within the plume. Again, this could be explained by the relatively small lateral extent of the injection volume. Importantly, however, the STM analysis illustrates the potential of ERT with respect to the quantification of transport heterogeneity.

4.4. Discussion of M_{0r} and M_{0a}

The fitted M_{0r} indicates that the increase in bulk electrical conductivity in the injection volume ($C_0 = 11.6$ g/l Br^-, $\sigma_{w,0} = 1.71$ S/m) is about 600–700% of the initial bulk electrical conductivity ($\sigma_{b,in} \approx 10$–15 mS/m). This corresponds well with the fitted M_{0a} (66 mS/m) which represents the absolute increase in σ_b in the injection volume. From Eq. (22) and the fitted M_{0a} and M_{0r}, the importance of the intercept b in the empirical relation between σ_b and σ_w (Eq. (14)) can be inferred. As discussed in Section 3.4, this intercept is related to the

Table 3
Mean, standard deviation, and uncertainty of fitted equivalent STM (Eq. (24)) parameters (Fig. 12). Standard deviation refers to the variability of the parameter in the analysed set of pixels and uncertainty to the average standard deviation of a parameter estimate in a pixel

	Mean	Standard deviation	Uncertainty
v_s (m/d)	1.07	0.14	0.03
λ_s (m)	0.33	0.10	0.06
M_{0s} (−)	1.18	0.54	0.07

interfacial conductivity σ_s. Solving Eq. (22) for b/a yields $b/a \approx 150-200\,\mathrm{mS/m}$. The ratio b/a represents the electrical conductivity of a solution that would lead to an increase in σ_b equal to the intercept b. Comparing this value with $\sigma_{w,in}$ (107.4 mS/m) and the relative changes of bulk electrical conductivity observed during breakthrough of the plume (up to about 100% of the initial bulk electrical conductivity), it is clear that it cannot be neglected. As a consequence, a calibration relation between σ_b and σ_w cannot be derived directly from the pair ($\sigma_{b,in}$, $\sigma_{w,in}$) assuming that $b \approx 0$. By solving Eq. (22) for both a and b/a, we obtain that $b \approx 5-8\,\mathrm{mS/m}$.

5. Summary and conclusions

We used ERT to monitor solute concentration changes on an ERT image plane during a tracer test. The obtained concentration images at selected time intervals were interpreted using equivalent transport models. We quantified the longitudinal and lateral spreading of the solute plume in terms of equivalent dispersivities of a 3D equivalent CDM. A 1D STM was used to quantify the observed heterogeneity of transport within the plume and the mixing process, which homogenises concentrations within the plume.

In order to use ERT-derived concentration distributions for quantitative analyses of subsurface solute transport, the smoothing effect, which results from standard regularisation to constrain the nonunique inverse problem, was quantified. Numerical experiments illustrated that smoothing may substantially influence the reconstructed concentration distributions. Especially parameters that quantify the dispersion and spreading process were found to be sensitive to the type of smoothing imposed. A relation between premised transport parameters and parameters recovered from the reconstructed images was derived on the basis of the numerical experiments. Using this relation in an inverse mode, estimated parameters from reconstructed images were roughly corrected for the smoothing effect that is inherent to the ERT imaging algorithm. The impact of smoothing on the reconstructed distributions varies across the ERT plane and is smaller in the sensitive region. As a consequence, the experimental setup (electrode arrangement and/or location of tracer injection) can be optimised so that the plume traverses the ERT plane in the most sensitive region. Besides the geometrical setup, also the ERT measurement schedule has a direct impact on the ultimate image resolution (Zhou and Greenhalgh, 2000) and, hence, should be taken into account. Also other criteria than the standard smoothness constraint may be considered

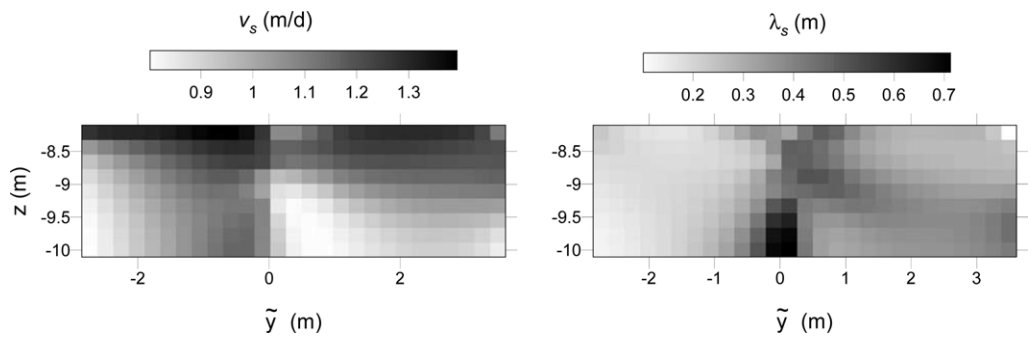

Fig. 12. Images of equivalent stream-tube velocity, v_s, and dispersivity, λ_s, as fitted to the recovered pixel breakthrough curves of relative bulk electrical conductivity change. Isotropic smoothing was used for regularisation in the underlying ERT inversions. Only the region of distinct tracer breakthrough is shown.

to regularise the inversion. Alternative approaches may be based on total variation methods, which have been shown to be capable of reconstructing relatively sharp structures (Yu and Dougherty, 2000), or state estimation principles, which enable to directly incorporate the physical nature of the process of interest into the inversion algorithm (Seppänen et al., 2001). However, it must be avoided that what is anticipated when defining a certain regularisation constraint is later derived or quantified from the reconstructed images.

Despite the important impact of smoothing or, more general, regularisation inherent to ERT imaging, ERT-derived concentration maps are especially useful to determine the spreading of the solute plume. When compared with traditional sampling in multilevel observation wells, the horizontal resolution of the ERT-derived concentration maps is much better than the resolution obtained with multilevel samplers, which is defined by the distance between the observation wells. For example, in this tracer test, the breakthrough of the salt tracer was observed in only two wells and it would be impossible to determine where the centre of mass of the plume traverses the ERT plane, let alone the lateral extent of the plume, using the multilevel observation wells.

The variability of equivalent parameters of the STM in the ERT image plane contains information about the spatial structure of the flow field. This information can be used to infer information about the structure of the hydraulic conductivity field (Rubin and Ezzedine, 1997; Vanderborght and Vereecken, 2001). Concentration maps with a high horizontal resolution are required to estimate the horizontal correlation scale of the hydraulic conductivity field. Assuming that the hydraulic conductivity field is isotropic in a horizontal plane, the correlation scale of the hydraulic conductivity in the horizontal direction of the mean flow may be estimated from concentration maps on a perpendicular (vertical) ERT plane. The correlation of the hydraulic conductivity in the direction of the mean flow is, together with the variance of the hydraulic conductivity, a key parameter for the spreading of a tracer plume in a heterogeneous aquifer. In this and a previous paper (Vanderborght and Vereecken, 2002), we quantified the mixing process by the equivalent dispersivity of locally observed BTCs, λ_s. However, other parameters that characterise the mixing process, e.g. dilution index (Kitanidis, 1994; Ursino et al., 2001), concentration variance and spatial covariance (Vanderborght, 2001), and local concentration gradients may be derived from concentration maps and coupled with properties of the medium that define the mixing process, i.e. the variance and spatial covariance of the hydraulic conductivity and the local-scale hydrodynamic dispersion.

With ERT, images of bulk electrical conductivity, σ_b, are obtained. Bulk electrical conductivity is related to the concentration of a salt tracer, C, but the calibration relation is likely to vary in the aquifer. Since it is impossible to derive a calibration relation between σ_b and C at each point, we made and tested some simplifying assumptions on a pragmatic basis. However, further research on the relation between σ_b and C is required to validate and evaluate these assumptions. A promising outlook in this context provides the induced polarisation (IP) method, where both electrical conduction and polarisation properties are measured. Since electrical polarisation phenomena are closely related to interfacial soil or rock characteristics, IP may help to reduce the explained ambiguity in the calibration relation. Recent advances with respect to both physico-chemical interpretation of observed effects (Lesmes and Frye, 2001) and development of efficient imaging techniques suitable for cross-borehole tomographic surveys (Kemna et al., 2000, 2002) make the application of the IP method in subsurface solute transport studies possible.

Acknowledgments

We are grateful to the company GeoServe (Kiel, Germany) for providing the ERT data acquisition system RESECS that was used in the field experiment. Michael Gräber (GeoServe) assisted us patiently in the start-up phase of the ERT field work. The chemical analysis of the multilevel groundwater samples was conducted by the Central Department of Analytical Chemistry (ZCH) of the Forschungszentrum Jülich GmbH,

which we appreciate very much. Last but not least, this work would not have been possible without the willing and able support by our colleagues at the Agrosphere Institute (ICG-IV) of the Forschungszentrum Jülich GmbH. In particular we would like to thank Rainer Harms, Andreas Englert, Odilia Esser, Horst Hardelauf, Felix Höpner, Frank Lamertz, Anke Langen, Dr Olaf Nitzsche, Hans G. Sittardt, Dr Olivier Smidts, and Sylvia de Waal for contributing to the successful realisation of the tracer experiment.

References

Alumbaugh, D.L., Newman, G.A., 2000. Image appraisal for 2-D and 3-D electromagnetic inversion. Geophysics 65, 1455–1467.

Archie, G.E., 1942. The electrical resistivity log as an aid in determining some reservoir characteristics. Trans. Am. Inst. Miner. Metall. Engng 146, 54–62.

Bevc, D., Morrison, H.F., 1991. Borehole-to-surface electrical resistivity monitoring of a salt water injection experiment. Geophysics 56, 769–777.

Binley, A., Ramirez, A.L., Daily, W.D., 1995. Regularised image reconstruction of noisy electrical resistance tomography data. In: Beck, M.S., Hoyle, B.S., Morris, M.A., Waterfall, R.C., Williams, R.A. (Eds.), Process Tomography, Proceedings of the 4th Workshop on European Concerted Action on Process Tomography, University of Manchester Institute of Science and Technology, 401–410.

Binley, A., Henry-Poulter, S., Shaw, B., 1996. Examination of solute transport in an undisturbed soil column using electrical resistance tomography. Water Resour. Res. 32, 763–769.

Bresler, E., Dagan, G., 1981. Convective and pore scale dispersive transport in unsaturated heterogeneous fields. Water Resour. Res. 17, 1683–1693.

Cirpka, O.A., Kitanidis, P.K., 2000a. An advective dispersive stream tube approach for the transfer of conservative tracer data to reactive transport. Water Resour. Res. 36, 1209–1220.

Cirpka, O.A., Kitanidis, P.K., 2000b. Characterization of mixing and dilution in heterogeneous aquifers by means of local temporal moments. Water Resour. Res. 36, 1221–1236.

Dagan, G., 1988. Time-dependent macrodispersion for solute transport in anisotropic heterogeneous aquifers. Water Resour. Res. 24, 1491–1500.

Dagan, G., 1989. Flow and Transport in Porous Formations, Springer, New York.

Daily, W.D., Ramirez, A.L., LaBrecque, D.J., Nitao, J., 1992. Electrical resistivity tomography of vadose water movement. Water Resour. Res. 28, 1429–1442.

Daily, W.D., Ramirez, A.L., LaBrecque, D.J., Barber, W., 1995. Electrical resistance tomography experiments at the Oregon Graduate Institute. J. Appl. Geophys. 33, 227–237.

Ellis, R.G., Oldenburg, D.W., 1994. Applied geophysical inversion. Geophys. J. Int. 116, 5–11.

Freyberg, D.L., 1986. A natural gradient experiment on solute transport in sand aquifer: 2. Spatial moments and the advection and dispersion of nonreactive tracers. Water Resour. Res. 22, 2031–2046.

Garabedian, S.P., LeBlanc, D.R., Gelhar, L.W., Celia, M.A., 1991. Large-scale natural gradient tracer test in sand and gravel, Cape Cod, Massachusetts: 2. Analysis of spatial moments for a nonreactive tracer. Water Resour. Res. 27, 911–924.

Ginn, T.R., Simmons, C.S., Wood, B.D., 1995. Stochastic-convective transport with non-linear reaction: 2. Biodegradation with microbial growth. Water Resour. Res. 31, 2689–2700.

deGroot-Hedlin, C., Constable, S.C., 1990. Occam's inversion to generate smooth, two-dimensional models from magnetotelluric data. Geophysics 55, 1613–1624.

Jensen, K.H., Bitsch, K., Bjerg, P.J., 1993. Large-scale dispersion experiments in a sandy aquifer in Denmark: observed tracer movements and numerical analyses. Water Resour. Res. 29, 673–696.

Johnson, D.L., Koplik, J., Schwartz, L.M., 1986. New pore-size parameter characterizing transport in porous media. Phys. Rev. Lett. 57, 2564–2567.

Kemna, A., 2000. Tomographic Inversion of Complex Resistivity: Theory and Application, Der Andere Verlag, Osnabrück.

Kemna, A., Binley, A., Ramirez, A.L., Daily, W.D., 2000. Complex resistivity tomography for environmental applications. Chem. Engng J. 77, 11–18.

Kemna, A., Binley, A., Slater, L., 2002. Cross-borehole IP imaging for engineering and environmental applications. Geophysics, Submitted for publication.

Kitanidis, P.K., 1994. The concept of the dilution index. Water Resour. Res. 30, 2011–2026.

LaBrecque, D.J., Yang, X., 2000. Difference inversion of ERT data: a fast inversion method for 3-D in-situ monitoring. Proc. Symp. Appl. Geophys. Engng Environ. Problems, Environ. Engng Geophys. Soc., 723–732.

LaBrecque, D.J., Miletto, M., Daily, W.D., Ramirez, A.L., Owen, E., 1996. The effects of noise on Occam's inversion of resistivity tomography data. Geophysics 61, 538–548.

Lesmes, D.P., Frye, K.M., 2001. The influence of pore fluid chemistry on the complex conductivity and induced-polarization responses of Berea sandstone. J. Geophys. Res. 106, 4079–4090.

Morris, M., Rønning, J.S., Lile, O.B., 1996. Geoelectric monitoring of a tracer injection experiment: modeling and interpretation. Eur. J. Environ. Engng Geophys. 1, 15–34.

Naff, R.L., Haley, D.F., Sudicky, E.A., 1998. High-resolution Monte Carlo simulation of flow and conservative transport in heterogeneous porous media: 2. Transport results. Water Resour. Res. 34, 679–697.

Osiensky, J.L., Donaldson, P.R., 1995. Electrical flow through an aquifer for contaminant source leak detection and delineation of plume evolution. J. Hydrol. 169, 243–263.

Ramirez, A.L., Daily, W.D., LaBrecque, D.J., Owen, E., Chesnut, D., 1993. Monitoring an underground steam injection process

using electrical resistance tomography. Water Resour. Res. 29, 73–87.

Revil, A., Glover, P.W.J., 1998. Nature of surface electrical conductivity in natural sands, sandstones, and clays. Geophys. Res. Lett. 25, 691–694.

Rhoades, J.D., Manteghi, N.A., Shouse, P.J., Alves, W.J., 1989. Soil electrical conductivity and soil salinity: new formulations and calibrations. Soil Sci. Soc. Am. J. 53, 433–439.

Rink, M., Schopper, J.R., 1974. Interface conductivity and its implication to electric logging. Transactions of the 15th Annual Logging Symposium, Soc. Prof. Well Log Analysts, 1–15.

Rubin, Y., Ezzedine, S., 1997. The travel time of solutes at the Cape Cod tracer experiment: data analysis, modeling, and structural parameter inference. Water Resour. Res. 33, 1537–1547.

SAS Institute Inc., 1989. SAS/STAT® User's Guide, Version 6, Fourth Edition, Volume 2. SAS Institute Inc., Cary, NC.

Sen, P.N., Goode, P.A., 1992. Influence of temperature on electrical conductivity on shaly sands. Geophysics 57, 89–96.

Sen, P.N., Goode, P.A., Sibbit, A., 1988. Electrical conduction in clay bearing sandstones at low and high salinities. J. Appl. Phys. 63, 4832–4840.

Seppänen, A., Vauhkonen, M., Vauhkonen, P.J., Somersalo, E., Kaipio, J.P., 2001. State estimation with fluid dynamical evolution models in process tomography: an application to impedance tomography. Inverse Problems 17, 467–483.

Simmons, C.S., 1982. A stochastic-convective transport representation of dispersion in one-dimensional porous media systems. Water Resour. Res. 18, 1193–1214.

Slater, L., Binley, A., Brown, D., 1997. Electrical imaging of fractures using ground-water salinity change. Groundwater 35, 436–442.

Slater, L., Binley, A., Daily, W.D., Johnson, R., 2000. Cross-hole electrical imaging of a controlled saline tracer injection. J. Appl. Geophys. 44, 85–102.

Ursino, N., Gimmi, T., Flühler, H., 2001. Dilution of non-reactive tracers in variably saturated sandy structures. Adv. Water Res. 24, 877–885.

Vanderborght, J., 2001. Concentration variance and spatial covariance in second order stationary heterogeneous conductivity fields. Water Resour. Res. 37, 1893–1912.

Vanderborght, J., Vereecken, H., 2001. Analyses of locally measured bromide breakthrough curves from a natural gradient tracer experiment at Krauthausen. J. Contam. Hydrol. 48, 23–43.

Vanderborght, J., Vereecken, H., 2002. Estimation of local scale dispersion from local breakthrough curves during a tracer test in a heterogeneous aquifer: the Lagrangian approach. J. Contam. Hydrol. 54, 141–171.

Vereecken, H., Döring, U., Hardelauf, H., Jaekel, U., Hashagen, U., Neuendorf, O., Schwarze, H., Seidemann, R., 2000. Analysis of solute transport in a heterogeneous aquifer: the Krauthausen field experiment. J. Contam. Hydrol. 45, 329–358.

Waxman, M.H., Smits, L.J.M., 1968. Electrical conductivities in oil-bearing shaly sands. Soc. Petrol. Engng J. 8, 107–122.

White, P.A., 1988. Measurement of ground-water parameters using salt-water injection and surface resistivity. Groundwater 26, 179–186.

White, P.A., 1994. Electrode arrays for measuring groundwater flow direction and velocity. Geophysics 59, 192–201.

Yu, M., Dougherty, D.E., 2000. Modified total variation methods for three-dimensional electrical resistance tomography inverse problems. Water Resour. Res. 36, 1653–1664.

Zhou, B., Greenhalgh, S.A., 2000. Cross-hole resistivity tomography using different electrode configurations. Geophys. Prosp. 48, 887–912.